

Combinatorial Methods for Polymer Science

Carson Meredith, Georgia Institute of Technology, Atlanta, Georgia
Archie P. Smith, National Institute of Standards and Technology, Gaithersburg, Maryland
Alfred J. Crosby, National Institute of Standards and Technology, Gaithersburg, Maryland
Eric J. Amis, National Institute of Standards and Technology, Gaithersburg, Maryland
Alamgir Karim, National Institute of Standards and Technology, Gaithersburg, Maryland

Encyclopedia of Polymer Science and Technology
Copyright © 2002 by John Wiley & Sons, Inc. All rights reserved.
DOI: 10.1002/0471440264.pst069
Article Online Posting Date: October 15, 2002

Keywords: Combinatorial methods; library creation; synthesis; characterization; high throughput; materials research

Abstract

This article presents recent advances in which combinatorial methodologies have been used for efficient measurement of chemical and physical properties of polymers over large regimes of variable space. Methodologies for both synthesis and characterization allow for both materials discovery and discovery of new models and structure–processing–property relationships. Polymer synthesis with combinatorial methods relies primarily on reactant mixing and diversity to create discrete libraries for investigating reactant structure and composition variations. In the future, techniques will be developed to allow library variation in processing variables like temperature, UV exposure, and pressure during synthesis. Several recent developments are presented in the combinatorial characterization of polymers, using high throughput libraries of films and coatings. As examples, four novel techniques are developed for preparing continuous gradient polymer libraries with controlled variations in temperature, composition, thickness, and substrate surface energy. The use of these new library techniques facilitates characterization of polymer blend phase behavior, thin-film dewetting, block copolymer order–disorder transitions, and polymer adhesion.

1. Introduction

Fundamental research of the synthesis and characterization of polymeric materials is driven by their use in applications including structural materials, packaging, microelectronics, coatings, biomedical materials, and nanotechnology. Current trends demand finer control of chemistry, morphology, and surface topography at the micrometer and nanometer scales. To achieve these goals, there are increasing needs for the synthesis and processing of multicomponent mixtures, composites, and thin films. However, these systems are inherently complex due to the interactions of phase transitions, microstructure, interfaces, and transport behavior that occur during synthesis and processing. The synthesis of polymers by emulsion polymerization, for example, involves colloid chemistry, micellization, transport between phases, and complex rate

relationships. In the case of coatings and thin films, the mechanical and optical properties, microstructure, and phase and wetting behavior are sensitive and poorly understood functions of thickness. In addition to the complex phenomena involved in polymer synthesis and processing, there is a large variable space involving parameters whose effects often counteract one another. These include reactant composition and structure, synthetic sequence, solvent, temperature, annealing history, pressure, and thickness (eg, in films). Conventional microscopy, spectroscopy, and analytical tools for polymer synthesis and characterization were designed for one-sample-one-measurement utilization, and are suited for detailed characterization over a limited set of variable combinations. This conventional approach is preferred when the most relevant variable combinations are known a priori or can be reliably predicted from theory. However, the complex phenomena and large variable spaces present in multicomponent, multiphase, bioactive or thin-film polymers often exceed the capabilities of current theory and conventional measurements. Therefore, a strong need exists for experimental techniques capable of highly efficient synthesis and characterization of complex polymeric systems over large numbers of variable combinations.

Combinatorial methods (CM) use experimental design, library creation, high throughput screening, and informatics to efficiently and rapidly develop new materials and measure properties over large numbers of variable combinations (Fig. 1). This is accomplished by preparing samples not one at a time, but rather as sample “libraries” containing hundreds to thousands of variable combinations each. High throughput measurements of relevant chemical and physical properties, combined with informatic data analysis, allow efficient development of structure–processing–property relationships. The benefits include efficient characterization of novel regimes of thermodynamic and kinetic behavior (knowledge discovery) and accelerated development of functional materials (materials synthesis and discovery). Although historically applied to pharmaceutical research, there is an increasing interest in applying CM to materials science, as indicated by recent reports of combinatorial methodologies for a wide range of inorganic (1-8) and organic/polymeric materials (7, 9-24).

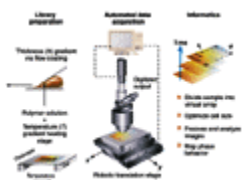


Figure 1. Schematic of the combinatorial experimental method, as applied to the preparation of thickness and temperature gradient film libraries, high throughput screening with optical microscopy, and informatic analysis of image data as a function of temperature, thickness, and time. Adapted with permission from Ref. 22.

Early combinatorial *materials* research used sputtering methods to prepare composition gradient libraries for measuring the phase behavior of ternary metal alloys (20) and other inorganic materials (25). However, limitations in computing capacity and instrument automation overshadowed the benefits of combinatorial materials' characterization until only recently. The primary limitation to *characterizing* polymers, as bulk material or films, with CM has been a shortage of techniques for preparing libraries with systematically varied composition (ϕ), morphology, physical form, thickness (h), and

temperature (T). This article is a review of recent advances in applying CM to polymer synthesis and characterization. Applications of CM to the synthesis of a wide range of polymeric materials, including sensors, dendrimers, and biodegradable polymer are presented. Several novel methods developed for the preparation of T , ϕ , h , and surface energy continuous polymer film libraries are discussed. There is particular focus on the novel library preparation and high throughput screening steps, since these have been the principal limiting factors in CM development for polymers. The use of continuous gradient libraries in the measurement of fundamental properties is described for polymer blend phase behavior, block copolymer segregation, and dewetting transitions.

2. Combinatorial Polymer Synthesis

Despite the recent increase in combinatorial inorganic materials research (2-7, 14, 15), there are still relatively few studies reporting CM for the synthesis of polymeric materials. One example is the work of Brocchini and co-workers (10, 11), where a 112-member combinatorial library of biodegradable polyarylates was prepared by copolymerizing all possible combinations of 14 tyrosine-based diphenols and 8 diacids. The pendant chain and backbone structures were systematically varied by the addition of methylene groups, substitution of oxygen for the methylene, and addition of branched or aromatic structures. The library products displayed diverse properties, as indicated by measurements of the glass-transition temperature T_g , air-water-contact angle (θ_w), and fibroblast proliferation during cell culture. Fibroblast proliferation was found to decrease with increased hydrophobicity except for the main-chain oxygen containing polymers that served as uniformly good growth substrates regardless of the hydrophobicity.

The results of the above study were utilized (13) to test informatic methods for designing *diverse* and *focused* combinatorial libraries. Molecular topology and genetic-algorithm-optimized quantitative structure-property relationships were used to design libraries. These techniques allowed selection of a representative subset of library members for rapid study of the entire library (a diverse subset) or concentration on a specific property of interest (a focused subset). Each monomer pair of the 112-member library was represented by a 2-D topological descriptor, used by the algorithm to select a structurally diverse and representative subset of the library. This subset was utilized to create models for the T_g and θ_w , which were tested by comparing to the T_g and θ_w of the entire library. Focused libraries of polymer structures predicted to meet certain T_g and θ_w specifications were also designed. Good agreement was reported between the calculated and experimental T_g and θ_w values, even for polymers not included in the subset library. Additionally, the focused libraries were shown to be effective in identifying polymer structures within specific T_g and θ_w ranges.

Gravert and co-workers (9) used parallel synthesis to design polymeric supports for liquid-phase organic synthesis. In this work, three polymerization initiators containing α -nitrile diazene cores were utilized for block copolymer synthesis, while a functionalized methacrylate initiator was used to produce graft copolymers. Five vinyl monomers were used in combination with the initiators to produce approximately 50 block and graft copolymers. Copolymer products were characterized by size exclusion chromatography,

nuclear magnetic resonance, and solubility in a range of solvents. Based upon this characterization, a 4-*tert*-butylstyrene-*b*-3,4-dimethoxystyrene block copolymer was selected and used successfully as a support in subsequent liquid-phase syntheses.

Takeuchi and co-workers (18) coupled combinatorial techniques with molecular imprinted polymers to develop sensors for triazine herbicides. The library consisted of a 7 × 7 array containing different fractions of monomers methacrylic acid (MAA) and 2-(trifluoromethyl)acrylic acid (TFMAA) with constant concentrations of the imprint molecules ametryn or atrazine. After UV-initiated polymerization, the products from the sensor library were characterized by HPLC measurement of herbicide concentration. The receptor efficiency was observed to vary with monomer type: the atrazine receptor efficiency increased with MAA composition and the ametryn receptor was enhanced by increased fractions of TFMAA. Although only monomer concentration was varied in the libraries, the authors conclude that the CM synthetic approach would be useful in analyzing other variables such as solvent, cross-linking agent, and polymerization conditions to produce optimum molecularly imprinted polymer sensors.

Dickinson and co-workers (12) reported CM synthesis of a sensor library consisting of solvatochromic dyes dissolved in polymer. Permeation of the polymer by volatile solvents induced changes in the dye's solvation environment, which were detectable by the fluorescence signal. A combination of methyl methacrylate and dimethyl(acryloxypropyl) methylsiloxane monomers was used to create two sensor libraries. A discrete library was prepared by photo-polymerizing constant concentration solutions of the dye and monomers to produce cones of polymer at different locations on the end of a fiber-optic bundle. A second, continuous library was created by adding methyl methacrylate to the copolymer monomer as UV light was scanned across the fiber-optic bundle, producing a copolymer concentration gradient across the bundle end. Both the discrete and the continuous libraries were characterized by monitoring the fluorescence response (via the fiber-optic cables) as a function of exposure to saturated organic vapors. The deposition of the library directly onto the measurement probe (fiber optic) makes this work a good example of a combined CM polymer synthesis and characterization. For the particular dye and monomer used, the fluorescence response was found to be a nonlinear function of the concentration.

Newkome and co-workers (26) report, a combinatorial strategy for synthesizing dendrimers with modified structure and surface chemistry. Mixtures of three branched isocyanate-based monomers, mixed over a wide range of compositions, were used to synthesize a combinatorial library of dendritic molecules. Based upon ¹³C NMR spectra, the dendrimer products displayed varying degrees of peripheral heterogeneity, adjustable by controlling the ratios of the three isocyanate monomer groups. The methodology provides for the rapid modification of dendritic properties based upon the chemistry and distribution of peripheral surface groups; for example, some of the dendrimers were amphiphilic, displaying solubility in CH₃OH, H₂O, and CHCl₃. The degree of amphiphilicity can be adjusted to favor solubilization in one of the solvents by varying the proportion of amino vs benzyl ether surface moieties, based upon the ratio of monomer building blocks.

3. Combinatorial Polymer Characterization

The previous section focused on CM studies in which the production or synthesis of new polymeric materials was the primary goal. In those examples the synthesis steps were combinatorial, but subsequent characterization steps were noncombinatorial. One exception is the fluorescent sensor libraries prepared on fiber-optic bundles, discussed above (12). In this section we describe library preparation and high throughput screening methods for the combinatorial *characterization* of both thick (≈ 1 to ≈ 50 μm) and thin (< 1 μm) polymer films and coatings. Here, the primary goal is not to produce new materials, but rather to use CM to measure relevant phase behavior, wetting, and microstructural properties over a large range of parameter combinations. The variables of primary importance in characterizing the physical and chemical properties of polymers in the bulk and film state include the composition in multicomponent mixtures and composites, thickness, temperature (eg, annealing, curing, melt processing), and substrate energy (γ_{so}).

While preparing polymer films and coatings libraries with variations in ϕ , h , T , and γ_{so} , we found that the deposition of films with continuous gradients in each of these properties is a convenient and practical alternative to the deposition of libraries containing discrete regimes. Of course the introduction of chemical, thickness, and thermal gradients drives non-equilibrium transport processes that will eliminate the gradients over time. The timescale and length scale over which gradient library measurements are valid are determined in part by the magnitude of these transport fluxes. In most cases high molecular mass ($M_w > 10,000$ g/mol) polymers have relatively low transport coefficients, eg, diffusivity and viscosity. (According to ISO 31-8, the term “molecular weight” has been replaced by “relative molecular mass,” symbol M_r . The conventional notation, rather than the ISO notation, has been employed for this publication.) Thus the mass transport and flow length scale and timescale are often orders of magnitude lower than those of the measurements, allowing properties to be measured near equilibrium.

3.1. Preparation of Polymer Coating and Thin-Film Libraries

3.1.1. Thickness Gradient Libraries

A velocity-gradient knife coater (21-24), depicted in Figure 1, was developed to prepare coatings and thin films containing continuous thickness gradients. A 50- μL drop of polymer solution (mass fraction 2–5%) was placed under a knife-edge with a stainless steel blade width of 2.5 cm, positioned at a height of 300 μm and at a 5° angle with respect to the substrate. A computer-controlled motion stage (Parker Daedal) moves the substrate under the knife-edge at a constant acceleration, usually 0.5–1 mm/s^2 . This causes the substrate coating velocity to gradually increase from 0 to a maximum value of 5–10 mm/s . The increase in fluid volume passing under the knife-edge with increasing substrate velocity results in films with controllable thickness gradients. Figure 2 shows h -gradients for polystyrene (PS) and blends of polystyrene/poly(vinylmethylether) (PS/PVME) films on Si substrates as a function of solution composition. Thin-film-thickness-dependent phenomena can be investigated from nanometers to micrometers employing several h -gradient films with overlapping

gradient ranges. One can verify that the relatively weak thickness and temperature gradients do not induce appreciable flow in the polymer film over the experimental time scale (21, 22). A unidirectional Navier–Stokes model for flow over a flat plate estimates lateral flow at a characteristic velocity of $1\ \mu\text{m}/\text{h}$ at $T = 135^\circ\text{C}$, in response to gravitational action on the thickness gradient (27). This small flow is orders of magnitude slower than the flow induced by the physical phenomena that these libraries are designed to investigate, such as dewetting (22) and phase separation (21). To check for flow, we examined thickness-gradient libraries before and after annealing at $T > T_g$, for a PS film ($M_w = 1800$) on Si/SiO_x (22). The difference of thickness gradients across the $2\ \text{cm} \times 3\ \text{cm}$ library area before and after annealing was within a standard uncertainty of $\pm 1.5\ \text{nm}$ (22).

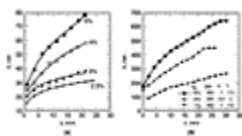


Figure 2. (a) Thickness, h (nm) vs distance x (mm) for various h -gradient film libraries composed of ($M_w = 1800\ \text{g/mol}$) on Si as a function of mass fraction PS in the toluene coating solution. (b) h (nm) vs x (mm) for h -gradient libraries of mass fraction 20% PS ($M_w = 96,400\ \text{g/mol}$)/80% PVME ($M_w = 119,000\ \text{g/mol}$) blends on Si as a function of mass fraction polymer composition in the toluene coating solution, blade substrate gap (μm), acceleration A (mm/s^2), and velocity (mm/s). Standard uncertainty in thickness is $\pm 3\ \text{nm}$. Figure 2a adapted with permission from Ref. 22.

3.1.2. Composition Gradient Libraries

Three steps are involved in preparing composition gradient films: gradient mixing (Fig. 3a), gradient deposition (Fig. 3b), and film spreading (Fig. 3c). Gradient mixing utilizes two syringe pumps (Harvard PHD2000) that introduce and withdraw polymer solutions (of mass fraction $x_A = x_B = 0.05\text{--}0.10$) to and from a small mixing vial at rates I and W , respectively. (Certain equipment and instruments or materials are identified in the article in order to adequately specify the experimental details. Such identification does not imply recommendation by the National Institute of Standards and Technology, nor does it imply the materials are necessarily the best available for the purpose.) Pump W was used to load the vial with an initial mass M_0 of solution B of $M_0 \approx 1\ \text{g}$. The infusion and withdrawal syringe pumps were started simultaneously under vigorous stirring of the vial solution, and a third syringe, S , was used to manually extract $\approx 50\ \mu\text{L}$ of solution from the vial into the syringe needle at the rate of $S = 30\text{--}50\ \mu\text{L}/\text{min}$. At the end of the sampling process, the sample syringe contained a solution of polymers A and B with a gradient in composition ∇x_A along the length of the syringe needle. The relative rates of I and W were used to control the steepness of the composition gradient, eg, dx_A/dt . The sample time, t_s , determines the endpoint composition of the gradient. The gradient produced by a particular combination of I , W , S , M_0 , and t_s values was modeled by a mass balance of the transient mixing process, given elsewhere (21). This balance predicts that the composition gradient will be linear only if $I = (W + S)/2$, a prediction supported by FTIR measurements of composition. An 18-gauge needle long enough to contain the sample volume ensured that the gradient solution did not enter the syringe

itself. This prevented turbulent mixing that might occur upon expansion of the solution from the needle into the larger diameter syringe.

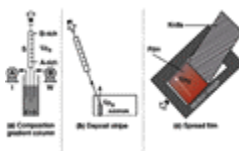


Figure 3. Schematic of the composition gradient deposition process involving (a) gradient mixing, (b) deposition of stripe, and (c) film spreading. Adapted with permission from Ref. 21.

Under the influence of the gradient in the syringe needle, ∇x_A , molecular diffusion will homogenize the composition. However, the timescale for molecular diffusion is many orders of magnitude larger than the sampling time. For example, consider gradient solutions of PS ($M_w = 96.4$ kg/mol, $M_w/M_n = 1.01$, Tosoh Inc.) and PVME ($M_w = 119$ kg/mol, $M_w/M_n = 2.5$) in toluene, a system used to characterize the ϕ -gradient deposition procedure (21, 28). For a typical ϕ -gradient with $\delta\phi \approx 0.025$ mm⁻¹, ϕ_{PS} and ϕ_{PVME} change negligibly by 0.004 and 0.001% in the 5-min period required for film deposition (21). [The diffusive flow rate of PS and PVME were calculated as $J = L \pi r^2 D_i \rho (d\phi_i/dx)_{\max}$, where ρ is the solution density, $r = 2.3$ mm is the syringe diameter, and $L = 4.2$ mm is the length of the fluid column in the syringe. We estimate $\delta\phi_i$ as $(Jt)/(x_p L \pi r^2 \rho)$, where $x_p = 0.08$ is the total polymer mass fraction in solution.] Fluid flow in the sample syringe remains in the laminar regime, preventing turbulence and convective mixing, discussed elsewhere (21).

The next library preparation step (Fig. 3b) is to deposit the gradient solution from the sample syringe as a thin stripe, usually 1–2-mm wide, on the substrate. This gradient stripe was spread as a film (Fig. 3c) orthogonal to the composition gradient, using the knife-edge coater described above. After a few seconds most of the solvent evaporated, leaving behind a thin film with a gradient of polymer composition. The remaining solvent was removed under vacuum during annealing, described in the next section (T -gradient annealing). Because polymer melt diffusion coefficients D are typically of order 10^{-12} cm²/s, diffusion in the cast film can be neglected if the lengthscale resolved in measurements is significantly larger than the diffusion length \sqrt{Dt} .

Composition gradient films of blends of PS/PVME and poly(D,L-lactide) (PDLA, Alkermes, Medisorb 100DL, $M_w = 127,000$ g/mol, $M_w/M_n = 1.56$)/poly(ϵ -caprolactone) (PCL, Aldrich, $M_w = 114,000$ g/mol, $M_w/M_n = 1.43$) were used to test the ϕ -gradient procedure. FTIR spectra were measured with a Nicolet Magna 550 and were averaged 128 times at 4 cm⁻¹ resolution. The beam diameter, 500 μ m (approximate), was significantly larger than the diffusion length of 3 μ m (approximate) for the experimental timescale. Films 0.3–1 μ m thick were coated on a sapphire substrate and a translation stage was used to obtain spectra at various positions on the continuous ϕ -gradient.

Figure 4a shows typical FTIR spectra for a ϕ -gradient film of PS/PVME. As position is scanned along the film, a monotonic increase in PVME absorbances, and a corresponding decrease in PS absorbances is observed. For the PS/PVME blend,

compositions were measured based upon a direct calibration of the $\nu = 2820 \text{ cm}^{-1}$ peak by using known mixtures, yielding $\nu(2820 \text{ cm}^{-1}) = (226 \pm 3)[\epsilon = A/hc, \text{ where } A \text{ is the absorbance for this peak, } h \text{ is the film thickness measured in micrometers, and } c \text{ is the molar density of PVME in moles per liter.}]$ For PDLA/PCL system, $\epsilon(\nu)$ values for pure PDLA and PCL were determined over the C-H stretch regime of $2700\text{--}3100 \text{ cm}^{-1}$, based upon $\epsilon_i(\nu) = A_i(\nu)/(ch)$, where A_i is the absorbance for each peak. Unknown PDLA/PCL mass fractions were determined to be within a standard uncertainty of 4% by assuming the observed spectra were linear combinations of pure PDLA and PCL spectra, eg, $A_{\text{mix}} = h(\alpha\epsilon_{\text{PDLA}}c_{\text{PDLA}} + (1-\alpha)\epsilon_{\text{PCL}}c_{\text{PCL}})$ and α is related to the mass fraction PDLA. Figure 4b shows typical composition gradients for PDLA/PCL blends coated from CHCl_3 and PS/PVME blends coated from toluene. Essentially linear gradients were obtained and the endpoints and slope agree with those predicted from mass balance (21). It is possible to create gradient films with wider composition ranges than those shown in Figure 5, by sampling the mixing vial for longer times (Fig. 4a).

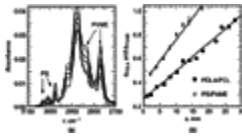


Figure 4. (a) FTIR spectra at $X = 2, 4, 8, 10, 14, 18 \text{ mm}$ positions along a ϕ -gradient PS/PVME library, as described in the text. PS absorptions decrease while PVME absorptions increase, monotonically, as one samples spectra across the film (increasing X (mm)). (b) Mass fractions ϕ_{PVME} and ϕ_{PCL} vs position x (mm) for typical PCL/PDLA and PS/PVME ϕ -gradient libraries. Composition of PS/PVME blends is calculated by calibration of the $\nu = 2820 \text{ cm}^{-1}$ PVME absorption. Composition in PDLA/PCL blends is calculated by the methodology described in the text. Coating parameters were PS/PVME ($I = 0.51 \text{ mL/min}$, $W = 1.0 \text{ mL/min}$, $S = 20 \text{ }\mu\text{L/min}$, $M_0 = 1.57 \text{ mL}$, sample time = 94 s) and PDLA/PCL ($I = 0.76 \text{ mL/min}$, $W = 1.5 \text{ mL/min}$, $S = 26 \text{ }\mu\text{L/min}$, $M_0 = 1.5 \text{ mL}$, sample time = 95 s) Unless otherwise indicated by error bars, standard uncertainty is represented by the symbol size. Figure 4b adapted with permission from Ref. 21.

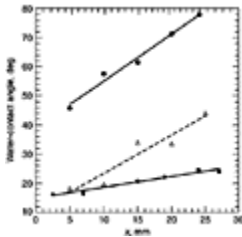


Figure 5. Deionized water-contact angle vs position (mm) for gradient-etched SiH/Si substrates as a function of both immersion rate and Piranha solution H_2SO_4 composition. Immersion rate and mass fraction H_2SO_4 are as follows: circles, 2.0 mm/s and 30%; triangles, 0.1 mm/s and 30%; diamonds, 2.0 mm/s and 40%. Standard uncertainty in contact angle is $\pm 2^\circ$.

3.1.3. Temperature Gradient Libraries

To explore a large T range, h - or ϕ -gradient films are annealed on a T -gradient heating stage, with the T -gradient *orthogonal* to the h - or ϕ -gradient. This custom aluminum T -gradient stage, shown in Figure 1, uses a heat source and a heat sink to produce a linear gradient ranging between adjustable end-point temperatures. End-point temperatures typically range from $(160 \pm 0.5)^\circ\text{C}$ to $(70.0 \pm 0.2)^\circ\text{C}$ over 40 mm, but are adjustable within the limits of the heater, cooler, and maximum heat flow through the aluminum plate. To minimize oxidation and convective heat transfer from the substrate, the stage is sealed with an o-ring, glass plate, and vacuum pump. Each 2-D T - h or T - ϕ parallel

library contains about 1800 or 3900 state points, respectively, where a “state point” is defined by the T , h , and ϕ variation over the area of a 200 \times optical microscope image: $\delta T = 0.5^\circ\text{C}$, $\delta h = 3 \text{ nm}$, and $\delta\phi = 0.02$. These libraries allow T , h , and ϕ -dependent phenomena, eg, dewetting, order–disorder, and phase transitions, to be observed *in situ* or postannealing with relevant microscopic and spectroscopic tools.

3.1.4. Surface Energy Gradients

In many polymer coating and thin-film systems, there is considerable interest in studying the film stability, dewetting, and phase behavior on substrates with surface energies varying between hydrophilic and hydrophobic extremes. Therefore, a gradient-etching procedure has been developed in order to produce substrate libraries with surface energy, γ_{so} , continuously varied from hydrophilic to hydrophobic values (29). The gradient-etching procedure involves immersion of a passivated Si-H/Si substrate (Polishing Corporation of America) into a 80 $^\circ\text{C}$ Piranha solution (30) at a *constant immersion rate*. The Piranha bath etches the Si-H surface and grows an oxide layer, SiO_x/SiOH , at a rate dependent on T and the volume fraction H_2SO_4 (30). A gradient in the conversion to hydrophilic SiO_x/SiOH results because one end of the wafer is exposed longer to the Piranha solution. After immersion, the wafer is withdrawn rapidly ($\approx 10 \text{ mm/s}$), rinsed with deionized water, and blown dry with N_2 . Typical deionized water contact angles are shown in Figure 5. By preparing several gradient substrates covering overlapping ranges of hydrophilicity, it is possible to screen a large range in surface energy, from hydrophilic ($\theta_w \approx 0^\circ$) to hydrophobic ($\theta_w \approx 90^\circ$) values of the water-contact angle.

In another procedure for varying substrate energy, developed by other authors, mixed self-assembled monolayers (SAMs) of alkanethiolates are deposited with a composition gradient (31). In this procedure, ω -substituted alkanethiolates with different terminal groups, eg, $-\text{CH}_3$ vs $-\text{COOH}$, cross-diffuse from opposite ends of a polysaccharide matrix deposited on top of a gold substrate. Diffusion provides for the formation of a SAM with a concentration gradient between the two thiolate species from one end of the substrate to another, resulting in controllable substrate energy gradients. The polysaccharide matrix is removed after a period of time, halting the diffusion process. These gradient SAM substrates were subsequently used to investigate the effect of surface energy on phase separation of immiscible polymer blends (32).

3.2. Uncertainty and Statistical Considerations of Library Measurements

A *potential drawback* of the method is that the polymer libraries are not composed of distinct sample areas, but rather have continuous gradients in ϕ , annealing T , and thickness h . These gradients induce variance in observed properties, which is not an issue with uniform samples. Many properties measured with combinatorial libraries are obtained from microscope images (optical, fluorescent, AFM, FTIR) or spectroscopy (UV, FTIR). Thus it is important to understand how uncertainties associated with the gradients and the lateral resolution affect properties measured on the libraries. Figure 6 demonstrates how a combinatorial library is divided into a grid of “virtual” measurement sites (eg, microscope images) of length scale L . The T and ϕ for each measurement site is taken as the average $\langle T \rangle$ and $\langle \phi \rangle$ over the length L . Because gradients are present on the library, each measurement site has systematic variances, $\delta\phi$

and δT , that increase as the measurement length scale L increases. Hence, lower measurement resolution (lower L) results in lower $\delta\phi$ and δT . A typical $500 \mu\text{m} \times 500 \mu\text{m}$ image would have reasonable variances of $\delta\phi = 0.01$ and $\delta T = 0.3^\circ\text{C}$. When measuring features within a site, the number of features sampled decreases as L decreases, causing an increase measurement uncertainty.

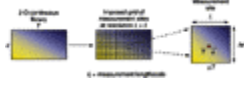


Figure 6. Distribution of discrete measurement sites of resolution $L \times L$ over a continuous gradient library. Measurement sites have average T and ϕ with gradient variance δT and $\delta\phi$.

How to select the optimum measurement scale L , reflecting a balance between counting statistics, $\delta\phi$ and δT ?

The effects of these contributions on the variance about the mean of any property $\langle p \rangle$ within a measurement site is accounted for using a standard uncertainty propagation,

$$\Delta\langle p \rangle = (\partial\langle p \rangle / \partial N)\Delta N + (\partial\langle p \rangle / \partial T)\Delta T + (\partial\langle p \rangle / \partial \phi)\Delta\phi \quad (1)$$

Here $\langle p \rangle$ is a function of T , ϕ , and the number of observations made in the measurement site, $N \sim L^2$. It is assumed that the number of features (microstructures, cells, etc) can be counted exactly, so that $\delta N = 0$. The partial derivatives can be estimated from finite difference approximations of the measured data, eg, $\partial \langle p \rangle / \partial T = [\sum p(T_{i+1}, \phi_i) - \sum p(T_i, \phi_i)] / [N(T_{i+1} - T_i)]$. The values of $\delta\phi$ and δT are $\delta\phi = m_\phi L$ and $\delta T = m_T L$, where m_T and m_ϕ are the slopes of the linear gradients, known from the library preparation procedure. Making these substitutions shows that the error propagation for property p scales as

$$\Delta\langle p \rangle \sim (m_T + m_\phi) / L \quad (2)$$

Constants have been removed from the above equation in order to reveal only the dependence on gradients and the measurement scale L . Equation 1 demonstrates that the uncertainty of any property measured on the libraries at a given ϕ and T will decrease if the measurement scale L is increased (because more features are counted) and if the magnitude of the gradients are decreased (reducing ϕ and T uncertainty). Thus the following guidelines should be followed during experimental design and data analysis: (1) L should be made as large as possible while still being able to resolve features of interest and (2) the gradient slopes should then be adjusted to attain an acceptable uncertainty (<1%) in the measured property. The analysis above considers only uncertainty contributions from the library gradients. Additional sources of uncertainty, arise from the measurements themselves, but these are also present for uniform conventional samples.

3.3. Fundamental Property Measurement with Combinatorial Polymer Coating and Film Libraries

3.3.1. Thin-Film Dewetting

Figure 7 shows a composite of optical microscope images of a T - h library of PS (Goodyear, $M_w = 1900$ g/mol, $M_w/M_n = 1.19$) on a SiO_x/SiOH substrate (22). The thickness ranges from 33–90 nm according to $h = 33.1x^{0.30}$ ($1 < x < 28$) mm and $85^\circ\text{C} < T < 135^\circ\text{C}$. The images, taken 2 h after initiation of dewetting, show wetted and dewetted regimes that are visible as dark and bright regions, respectively, to the unaided eye. Repeated examination of combinatorial T - h libraries at thicknesses ranging from 16–90 nm indicates three distinct thickness regimes with different hole nucleation mechanisms. For $h > 55 \pm 4$ nm, discrete circular holes in the film nucleate via heterogeneities (eg, dust) and grow at a rate dependent on T (quantification of the rate is given in Fig. 8).

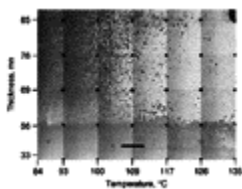


Figure 7. Composite of optical images of a T - h combinatorial library of PS ($M_w = 1800$ g/mol) on silicon, $t = 2$ h, $25\times$ magnification. Scale bar = 2.0 ± 0.1 mm. The thickness scale is a power law function (given in text), reflecting the nonlinear thickness gradient deposition procedure. Adapted with permission from Ref. 22.

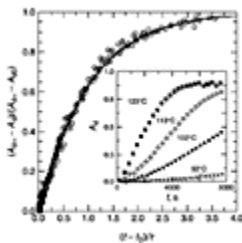


Figure 8. T - h - t superposition of dewet area fraction data onto a universal curve, $92^\circ\text{C} < T < 135^\circ\text{C}$, $59 \text{ nm} < h < 86 \text{ nm}$. Inset: raw dewet area fraction vs time, $h = 79$ nm. Adapted with permission from Ref. 22.

Below $h \leq 55 \pm 4$ nm, there is a sharp and temperature independent transition to a regime where irregular, asymmetrical holes nucleate and grow more slowly than at $h > 55$ nm. In the regime $33 \text{ nm} < h < 55$ nm, the heterogeneous and capillary instability nucleation mechanisms compete. The asymmetrical holes present in this regime are surrounded by bicontinuous undulations in the film surface, with a characteristic spacing of $7 \mu\text{m}$, as indicated by optical microscopy (22). AFM indicates a roughened surface with correlated surface undulations. A similar structure consisting of asymmetrical holes that breakup into a bicontinuous pattern at late stage, termed an “intermediate morphology,” has been observed recently for 12-nm-thick films of poly(styrene-*ran*-acrylonitrile) (33). Below $h \approx 33$ nm, another transition in structure and nucleation is apparent. Here, holes are nucleated by capillary instability and grow more quickly than in the region $33 \text{ nm} < h < 55$ nm.

Systematic studies of the temperature dependence of dewetting rates have not been reported to our knowledge. However, through its effect on viscosity, T is expected to have a strong influence on hole drainage rates. By using automated optical microscopy

(Fig. 1), a 5×5 grid of images covering the T and h range of the library was collected every 5 min for 2 h. Automated image analysis (22) of hole area as a function of T , h , and t assays a broad range of dewetting rates in a single experiment, shown in Figure 8. The inset to Figure 8 shows the raw dewetted area fraction A_d vs t at various temperatures from the T - h library for $h = 79$ nm. The entire set of A_d vs t profiles for $h > 55$ nm can be fitted with $A_d = A_{d\infty} + (A_{d0} - A_{d\infty}) \exp[-(t-t_0)/\tau]$, where A_{d0} and $A_{d\infty}$ are the dewet fractions at $t = t_0$ and $t = \infty$, τ is the dewetting time constant, and t_0 is a time delay for nucleation. As shown in Figure 8, in reduced units of $(A_{d\infty} - A_d)/(A_{d\infty} - A_{d0})$ vs $(t - t_0)/\tau$, the hole drainage profiles collapse onto the universal exponential curve given above. Figure 8 contains T and h data over a large range $92^\circ\text{C} < T < 135^\circ\text{C}$ and $59 \text{ nm} < h < 86 \text{ nm}$, and τ ranges from 2100 s (high temperatures) to 113,000 s (low temperatures). This T - h superposition for dewetting rates, previously unreported, reflects variations in the film viscosity with T and h , and could be missed altogether by relying solely upon limited numbers of samples.

3.3.2. Phase Behavior

Figure 9 presents a photograph of a typical temperature–composition library of the PS/PVME blend (discussed under Composition Gradient Libraries) after 90 min of annealing. As Figure 9 indicates, the lower critical solution temperature (LCST) cloud point curve can be seen with the unaided eye as a diffuse boundary separating one-phase and two-phase regions. Cloud points measured on bulk samples with conventional light scattering are shown as discrete data points and agree well with the cloud point curve observed on the library (21, 34). The diffuse nature of the cloud point curve reflects the natural dependence of the microstructure evolution rate on temperature and composition. Near the LCST boundary the microstructure size gradually approaches optical resolution limits ($1 \mu\text{m}$), giving the curve its diffuse appearance. Based upon a bulk diffusion coefficient of $D \approx 10^{-17} \text{ m}^2/\text{s}$, the diffusion length (\sqrt{Dt}) for a 2h anneal is 270 nm. In Figure 9 each pixel covers about $30 \mu\text{m}$, which is over 100 times the diffusion length, and ϕ -gradient-induced diffusion has a negligible effect on the observed LCST cloud point curve. The combinatorial technique employing T - ϕ polymer blend libraries allows for rapid and efficient characterization of polymer blend phase behavior (cloud points) in orders of magnitude less time than with conventional light scattering techniques.

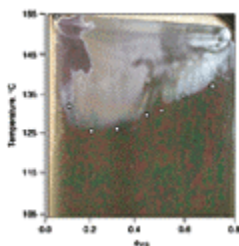


Figure 9. Digital optical photographs of a PS/PVME T - ϕ library after 90 min of annealing, showing the LCST cloud point curve visible to the unaided eye. The library wafer dimension is $31 \text{ mm} \times 35 \text{ mm}$ and the film thickness varies approximately 400–600 nm from low to high ϕ_{PS} values. White circles are light-scattering cloud points measured on separate uniform samples.

3.3.3. Block Copolymer Segregation and Surface Morphology

The morphology of symmetric diblock copolymer thin films has been studied extensively with traditional techniques (35-48). These studies found surface induced

formation of lamellae with thickness equal to the equilibrium lamellar thickness L_0 parallel to the substrate. The lamellae form smooth films when the total film thickness h is equal to an integral multiple m of L_0 , $h \approx mL_0$ for one block segregating to both the substrate and air interfaces and $h \approx (m + \frac{1}{2})L_0$ for one block preferring the substrate and the other preferring the air interface. When h deviates from these values, holes or islands of height L_0 are found to form on the film surface so as to reduce the system energy. Although there has been significant previous investigation of these systems, almost no research on the factors controlling the lateral dimensions of these surface features has been reported. In addition, no investigation of the transition regions between the hole and island formations has been performed due to the difficulty in accurately controlling film thickness with traditional spin-coating techniques. These types of questions are ideal for CM where it is possible to produce continuous h -gradient films of symmetric diblock copolymers with various molecular masses (23, 24).

Gradients in h of symmetric polystyrene-*b*-poly(methyl methacrylate) (PS-*b*-PMMA) with three different molecular masses were produced using the knife-edge flow coating technique described above. After characterization of h with UV-visible interferometry, the films were annealed at 170°C for up to 30 h to allow lamellar organization. The resulting morphologies were characterized with OM (optical microscopy) and AFM. Figure 10 presents a true color optical micrograph of a $M_w = 26,000$ g/mol gradient film showing morphological changes associated with the addition of two lamellae to the surface of the film. Labels denote approximate h values corresponding to $h \approx (m + \frac{1}{2})L_0$ for $m = 4, 5,$ and 6 . The morphology evolves from a smooth film to circular islands to a bicontinuous hole/island region to circular holes back to a smooth film from left to right in the micrograph and repeats twice. This morphology was observed to consistently repeat for h ranging from $2.0L_0$ to $6.5L_0$ for all molecular masses examined. Notably, the smooth regions of the film form a significant fraction of the morphology, corresponding to a thickness range δh deviating significantly from an integral multiple of L_0 . This δh is confirmed in the optical micrograph presented in Figure 10b where the smooth region of a $M_w = 104,000$ g/mol PS-*b*-PMMA gradient film is displayed. The orange features on the left are holes and the yellow-green features on the right are islands and the smooth region changes color from purple to blue-green indicating an h increase. The value of δh is $\approx 0.28L_0$ and invariant within standard uncertainty for all M_w and h investigated. This effect is interpreted to arise from a brush-like stretching and compression of block copolymer chains in the outer lamella as the chain density varies with h . Therefore islands and holes form only when the free energy penalty of chain deformation becomes so large that the defect structures are more energetically favorable.

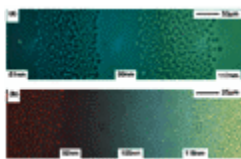
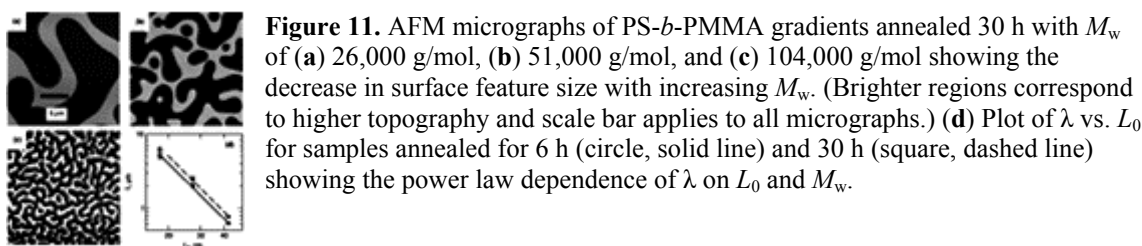


Figure 10. (a) Optical micrograph of a $M_w = 26,000$ g/mol PS-*b*-PMMA gradient film showing the addition of two lamellae to the surface. Labels indicate $h = 4.5L_0$, $5.5L_0$, and $6.5L_0$ for this M_r copolymer. (b) Optical micrograph of a $M_w = 104,000$ g/mol PS-*b*-PMMA gradient film showing the change in h across the smooth region. The color change from purple to blue-green indicates a δh of ≈ 25 nm across the smooth area. Standard uncertainty in thickness is ± 3 nm.

The lateral size of the surface patterns, which can be remarkably large when compared to L_0 or h , was also investigated using the h -gradient block copolymer film libraries. Figure 11 shows AFM micrographs of the surface of PS-*b*-PMMA gradient films with M_w of 26,000 g/mol (Fig. 11a), 51,000 g/mol (Fig. 11b), and 104,000 g/mol (Fig. 11c), annealed for 30 h at 170°C. These micrographs demonstrate that the lateral scale of the surface features decreases with increasing M_w . This fact is quantified by obtaining 2-D Fourier transforms of the micrographs (Fig. 11d) and extracting a characteristic peak wavevector (q^*) for each M_w . Figure 11d contains a plot of $\lambda \equiv (1/q^*)$ vs L_0 for samples annealed for both 6 h and 30 h and the lines correspond to power law fits yielding the relation $\lambda(\mu\text{m}) \sim L_0^{-2.5}$ or correspondingly $\lambda(\mu\text{m}) \sim M_w^{-1.5}$. This decrease of λ with increasing M_w suggests that as M_w of the outer block copolymer layer increases, its viscoelastic nature increases the free energy cost of forming large-scale surface patterns. The large-scale pattern formation in block copolymer films is therefore tentatively ascribed to the increased surface energy required to deform the surface of the block copolymer layers with increasing M_w .



3.3.4. Organic Light-emitting Diodes

We also mention here two characterization studies of the optimization of organic light emitting diodes (OLEDs). Schmitz and co-workers (14-16) used a masked deposition technique to produce thickness gradients in both the organic hole transport layers and the inorganic electron transport and emitting layer. OLEDs with single-gradient and orthogonal 2-D gradient structures were produced in order to evaluate the effects of the various layer thicknesses on the device efficiency. An optimal thickness for both the hole and electron transporting layers was reported. Likewise, Gross and co-workers (17) reported the use of CM to investigate the performance of doped (oxidized) ϕ -conjugated polymers in OLEDs. In these devices the polymers serve as hole transport layers but an energy barrier for hole injection exists between the polymeric material and the inorganic anode. By varying the oxidation level of the polymer this energy barrier can be reduced to lower the device working voltage. The effect of oxidation was studied by electrochemically treating the polymer to create a continuous gradient in the oxidation level of the polymer. A gradient in thickness was created orthogonal to the gradient in oxidation to explore variations of both properties simultaneously. For this reason, this study represents a cross between both combinatorial synthesis (oxidation steps) and process characterization (thickness gradient deposition). The gradient libraries were characterized by monitoring the efficiency and onset voltage of OLEDs fabricated on the gradients.

3.3.5. Combinatorial Adhesion Measurements

More recently, Crosby and co-workers (49) developed a combinatorial technique that can be used to investigate adhesive interactions between a polymer and another polymer, ceramic, or metal. The primary goal in the development of this technique was to design a high throughput, parallel processing adhesion test that allowed the adhesive strength dependence on multivariable environments to be determined. This combinatorial methodology for measuring polymer adhesion is largely built upon the theory of Johnson, Kendall, and Roberts (JKR) (50), which facilitates the measurement of the adhesive forces between two contacting surfaces. In the classical use of this theory, a hemispherical lens of one material is brought into contact with a complementary substrate, and subsequently separated. Rather than using a single hemispherical lens, Crosby and co-workers (49) used an array of microlenses (Fig. 12a). During this process, the contact area and displacement of each microlens is recorded through the use of an image-acquisition system integrated with an optical microscope. With these parameters, the JKR theory can then be used to quantify the adhesion energy between the two contacting materials (51). Along each axis of the array, a gradient in different environmental parameters or material properties can be placed. Examples of such gradient properties are surface energy, temperature, thickness, crosslink density, blend composition, and strain. If two orthogonal gradients are placed on the array, then each microlens contact point will yield a measurement of adhesion for a unique combination of parameters. The reported microlens libraries are capable of measuring 1600 different points of adhesion within a single test.

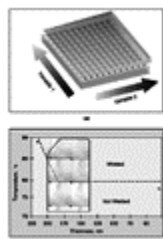


Figure 12. (a) Schematic of microlens array used in combinatorial JKR adhesion test with two parameters varying along orthogonal axis. (b) Experimental results from combinatorial JKR adhesion test displaying thickness dependence of critical welding temperature for polystyrene self-adhesion. Weld spots are visible features in image. The two isolated data points were collected from independent adhesion tests. Edges of microlens array are indicated by solid black lines.

This methodology is demonstrated by investigating the effect of thickness and temperature on the self-adhesion of PS. In this test, a microlens array was made from poly(dimethylsiloxane) (PDMS). Onto this PDMS array was floated a thin layer of PS containing a thickness gradient. The complementary substrate for this test was a PS-coated silicon wafer with an applied temperature gradient. During contact, the PS molecules diffused across the interface to entangle and strengthen the interface, thus causing the PS coating of the PDMS microlenses to delaminate within the contact regions. This “welding” of the contact areas occurs above a critical temperature and below a critical thickness over the time scale of the test (Fig. 12b). Such measurements are useful for the microelectronics industry where adhesion of thin-polymer layers determine the integrity of electronic packaging, but the general technique will have impact on the numerous industries where adhesion plays a dominant role.

Bibliography

1. E. Reddington, A. Sapienza, B. Gurau, R. Viswanathan, S. Sarangapani, E. Smotkin, and T. Mallouk, *Science* **280**, 1735 (1998).
2. X.-D. Xiang, X. Sun, G. Briceno, Y. Lou, K.-A. Wang, H. Chang, W. G. Wallace-Freedman, S.-W. Chen, and P. G. Schultz, *Science* **268**, 1738 (1995).
3. J. Wang, Y. Yoo, C. Gao, I. Takeuchi, X. Sun, H. Chang, X.-D. Xiang, and P. G. Schultz, *Science* **279**, 1712 (1998).
4. X.-D. Sun and X. X.-D. *Appl. Phys. Lett.* **72**, 525 (1998).
5. E. Danielson, J. H. Golden, E. W. McFarland, C. M. Reaves, W. H. Weinberg, and X. D. Wu, *Nature* **389**, 944–948 (1997).
6. E. Danielson, M. Devenney, D. M. Giaquinta, J. H. Golden, R. C. Haushalter, E. W. McFarland, D. M. Poojary, C. M. Reaves, W. H. Wenberg, and X. D. Wu, *Science* **279**, 837–839 (1998).
7. B. Jandeleit, D. J. Schaefer, T. S. Powers, H. W. Turner, and W. H. Weinberg, *Angew. Chem. Int. Ed.* **38**, 2494 (1999).
8. J. Klein, C. W. Lehmann, H.-W. Schmidt, and W. F. Maier, *Angew. Chem. Int. Ed.* **37**, 3369 (1998).
9. D. J. Gravert, A. Datta, P. Wentworth, and K. D. Janda, *J. Am. Chem. Soc.* **120**, 9481 (1998).
10. S. Brocchini, K. James, V. Tangpasuthadol, and J. Kohn, *J. Am. Chem. Soc.* **119**, 4553 (1997).
11. S. Brocchini, K. James, V. Tangpasuthadol, and J. Kohn, *J. Biomed. Mater. Res.* **42**, 66 (1998).
12. T. A. Dickinson, D. R. Walt, J. White, and J. S. Kauer, *Anal. Chem.* **69**, 3413 (1997).
13. C. H. Reynolds, *J. Comb. Chem.* **1**, 297 (1999).
14. C. Schmitz, P. Posch, M. Thelakkat, and H. W. Schmidt, *Phys. Chem. Chem. Phys.* **1**, 1777 (1999).
15. C. Schmitz, M. Thelakkat, and H. W. Schmidt, *Adv. Mater.* **11**, 821 (1999).
16. C. Schmitz, P. Posch, M. Thelakkat, and H. W. Schmidt, *Macromol. Symp.* **154**, 209 (2000).
17. M. Gross, D. C. Muller, H. G. Nothofer, U. Sherf, D. Neher, C. Brauchle, and K. Meerholz, *Nature* **405**, 661 (2000).
18. T. Takeuchi, D. Fukuma, and J. Matsui, *Anal. Chem.* **71**, 285 (1999).
19. N. K. Terrett, *Combinatorial Chemistry*, Oxford, Oxford, 1998.
20. K. Kennedy, T. Stefansky, G. Davy, V. F. Zackay, and E. R. Parker, *J. Appl. Phys.* **36**, 3808–3810 (1965).
21. Carson Meredith, A. Karim, and E. J. Amis, *Macromolecules* **33**, 5760–5762 (2000).
22. Carson Meredith, A. P. Smith, A. Karim, and E. J. Amis, *Macromolecules* **33**, 9747–

9756 (2000).

23. A. P. Smith, Carson Meredith, J. F. Douglas, E. J. Amis, and A. Karim, *Phys. Rev. Lett.* **87**, 015503 (2001).
24. A. P. Smith, J. F. Douglas, Carson Meredith, E. J. Amis, and A. Karim, *J. Polym. Sci., Part B: Polym. Phys.* **39**, 2141 (2001).
25. J. J. Hanak, *J. Mater. Sci.* **5**, 964 (1970).
26. G. R. Newkome, C. D. Weis, C. N. Moorefield, G. R. Baker, B. J. Childs, and J. Epperson, *Angew. Chem. Int. Ed.* **37**, 307–310 (1998).
27. L. G. Leal, *Laminar Flow and Convective Transport Processes*, Butterworth-Heinemann, Boston, 1992.
28. P. J. Daivis, D. N. Pinder, and P. T. Callaghan, *Macromolecules* **25**, 170–178 (1992).
29. K. Ashley, A. Sehgal, E. J. Amis, D. Raghavan, and A. Karim, MRS 2001 Fall Meeting Proceeding, in *Polymer Interfaces and Thin Films*, in press.
30. W. Kern, ed., *Handbook of Semiconductor Wafer Cleaning Technology*, Noyes Publications, Park Ridge, N.J., 1993.
31. B. Liedberg and P. Tengvall, *Langmuir* **11**, 3821–3827 (1995).
32. J. Genzer and E. J. Kramer, *Europhys. Lett.* **44**, 180–185 (1998).
33. J. L. Masson and P. F. Green, *J. Chem. Phys.* **112**, 349 (1999).
34. Carson Meredith, A. Tona, J.-L. Sormana, A. Garcias, A. Karim, and E. J. Amis, *J. Biomed. Mater. Res.*, in Press.
35. H. Hasegawa and T. Hashimoto, *Macromolecules* **8**, 589 (1985).
36. C. S. Henkee, E. L. Thomas, and L. J. Fetters, *J. Mater. Sci.* **23**, 1685 (1988).
37. T. P. Russell, G. Coulon, V. R. Deline and D. C. Miller, *Macromolecules* **22**, 4600 (1989).
38. P. F. Green, T. M. Christensen, T. P. Russell, and R. Jerome, *Macromolecules* **22**, 2189 (1989).
39. S. H. Anastasiadis, T. P. Russell, S. K. Satija, and C. F. Majkrzak, *J. Chem. Phys.* **92**, 5677 (1990).
40. D. Ausserre, D. Chatenay, G. Coulon, and B. Collin, *J. Phys. (France)* **51**, 2571 (1990).
41. G. Coulon, D. Ausserre, and T. P. Russell, *J. Phys. (France)* **51**, 777 (1990).
42. T. P. Russell, A. Menelle, S. H. Anastasiadis, S. K. Satija, and C. F. Majkrzak, *Macromolecules* **24**, 6263 (1991).
43. P. F. Green, T. M. Christensen, and T. P. Russell, *Macromolecules* **24**, 252 (1991).
44. T. P. Russell, A. Menelle, S. H. Anastasiadis, S. K. Satija, and C. F. Majkrzak, *Macromol. Chem., Macromol. Symp.* **62**, 157 (1992).
45. A. Menelle, T. P. Russell, S. H. Anastasiadis, S. K. Satija, and C. F. Majkrzak, *Phys. Rev. Lett.* **68**, 67 (1992).

46. Z. Cai, K. Huang, P. A. Montano, T. P. Russell, J. M. Bai, and G. W. Zajac, *J. Chem. Phys.* **93**, 2376 (1993).
47. G. Coulon, J. Daillant, B. Collin, J. J. Benattar, and Y. Gallot, *Macromolecules* **26**, 1582 (1993).
48. A. M. Mayes, T. P. Russell, P. Bassereau, S. M. Baker, and G. S. Smith, *Macromolecules* **27**, 749 (1994).
49. A. J. Crosby, A. Karim, and E. J. Amis, *Am. Chem. Soc. Polym. Prepr.* **42**, 645 (2001).
50. K. L. Johnson, K. Kendall, and A. D. Roberts, *Proc. R. Soc. London, Ser. A* **324**, 301–313 (1971).
51. K. R. Shull, D. Ahn, W.-L. Chen, C. M. Flanigan, and A. J. Crosby, *Macromol. Chem. Phys.* **199**, 489–511 (1998).